

1 **Please find a point-by-point discussion and answer of the issues raised by the reviewers.**
2 **To facilitate the work of reviewers and the editor, the reviewer's comments and**
3 **suggestions are preceding each reply in blue. The authors are grateful to referees for**
4 **their constructive remarks.**

5 **Referee #1**

6 Some details about the comparison of the profiles are missing.

7 Is the comparison done at the IASI L2 pressure level grid?

8 **Yes. We have added a sentence to be clearer:**

9 **“Note that vertical values for both r_{IASI} and r_{lidar} are used at the IASI-L2 pressure level**
10 **grid.”**

11 Have the lidar derived water vapour profiles been smoothed prior to the comparison?

12 **Yes. We have added a sentence to be clearer:**

13 **“The lidar profiles were smoothed for the comparison so that the vertical resolution**
14 **used for this study is ~41 m.”**

15 When comparing with ECMWF, why are the 9 closest model grid points being averaged
16 instead of, for example, using bilinear interpolation based on the 4 closest points (given the
17 high spatial variation of water vapour)?

18 **When checking the standard deviation computed on the 9 ECMWF grid it appears very**
19 **low for all the studied atmospheric situations. So, we have chosen to consider the mean**
20 **value in showing the standard deviation. We agree that when it is dispersed, it is**
21 **preferable to use a multiple-linear interpolation. In our case, the results are very close.**

22 The comparison shows the good correlation between the IASI and WALI water vapour
23 profiles above 2 km, but also highlights the disability of the IASI retrievals to capture strong
24 vertical gradients. The conclusion, rightly, mentions the higher spectral resolution offered by
25 the future IASI-NG instrument as an important way to improve the vertical resolution of the
26 water vapour retrievals. Additionally, the synergetic use of microwave measurements is
27 capable of improving the water vapour retrievals, especially in the PBL. An upcoming version
28 (6) of the operational IASI Level 2 processor with synergistic use of AMSU and MHS data
29 was announced at the International TOVS Study Conference earlier this year. It was reported
30 to contain substantial improvements of the profiles when compared with ECMWF analysis, in
31 particular in the lower levels and for the water vapour profiles. It would be interesting to
32 characterize to what degree these improvements can also be observed when comparing with
33 high vertical resolution reference profiles such as the ones presented in this paper.

34 **It is a good remark and we have added this point in the conclusion:**

35 **“Moreover, the synergetic use of microwave measurements is capable of improving the**
36 **water vapor retrievals, especially in the PBL. An upcoming version (6) of the**
37 **operational IASI Level 2 processor with synergistic use of the Advanced Microwave**
38 **Sounding Unit (AMSU) and the Microwave Humidity Sounder (MHS) data is scheduled.**
39 **It was reported to contain substantial improvements of the profiles when compared with**
40 **ECMWF analysis, in particular in the lower levels and for the entire water vapor**
41 **profiles.”**

42 **In another way, we are in contact with EUMETSAT to performed similar study with the**
43 **new products in development. Hence, we have added the sentence:**

44 **“The approach presented in this study can be applied to the next generation of IASI**
45 **operational water vapor products.”**

46

47 **Referee #2**

48 **Specific Comment**

49 **The main point is related to the lack of description of retrieval methodologies framework of**
50 **the IASI products used and cited in this paper. Even if the article does not aim to describe the**
51 **IASI H2O operational products, the authors should at least distinguish between results**
52 **obtained with statistical retrieval (such as EUMETSAT IASI L2 products) and physical**
53 **retrieval (i.e. Masiello et al. 2013 reference in the paper). In the literature it is widely known**
54 **that the former methodology has a poorer vertical resolution with respect to the latter.**

55 **As an example the authors can compare panel 11 of Figure 3 and Figure 9.a) of Masiello et al.**
56 **2013. In both cases the lidar sees a dry line around 2-5 km in agreement with ECMWF**
57 **analysis. But in the first case IASI product is smoother then lidar profile and does not see the**
58 **dry line, while in the second case IASI is capable to fit this kind of structure. The difference is**
59 **for sure related to the type of methodology behind the products: the first one uses a statistical**
60 **approach and the second one a physical retrieval scheme. This information should provide to**
61 **the reader a better description of the quality of vertical profiles derived from Hyperspectral**
62 **satellite measurements. In addition the authors, to state the capability of retrieving Water**
63 **Vapor mixing ratio profiles on a Global scale, cited Amato et al. 2009 paper. The**
64 **methodology described in this article is based on Statistical approach, while the dataset used**
65 **in this article has been processed with physical based methodology in another paper of the**
66 **same journal number (Masiello et al. 2009).**

67 **Yes, we agree with the referee and a brief description of the IASI products obtained**
68 **with statistical retrieval and physical retrieval has been added in our paper:**

69 **“Note that the operational product uses a statistical approach to retrieve the geophysical**
70 **parameters. Other approaches use a physical scheme and give access to a better vertical**
71 **resolution (e.g. Amato et al., 2009; Masiello et al., 2013). Nevertheless, the goal of this**

72 **paper is to provide quantitative elements of validation for the operational product using**
73 **the statistical approach.”**

74 **The reference to Amato et al. (2009) has been moved.**

75 The second point is related to the Introduction section. I find it is a bit unfair and misleading
76 that the authors dealt with history of Water vapor retrieval jumping from TIROS to TES
77 neglecting the heritage of the Japanese Fourier Transform Spectrometer IMG.

78 **Good remark, we have added the Japanese Fourier Transform Spectrometer IMG in**
79 **our introduction. In addition, we worked on the evaluation of this instrument before**
80 **launch. We have added the reference to Ogawa et al. (1994).**

81

82 [Minor point](#)

83 Reference Hilton et al. 2012 appears twice at pages 14089 and 14090. The second one seems
84 to be correct!

85 **We have deleted the first one which is wrong.**

86 | **Comparison of IASI water vapor retrieval with H₂O-Raman lidar in the frame of the**
87 | **Mediterranean HyMeX and ChArMEx programs**

88 | Patrick Chazette, Fabien Marnas, Julien Totems and Xiaoxia Shang

89 |
90 | Laboratoire des Sciences du Climat et de l'Environnement (LSCE), UMR8212, Laboratoire
91 | mixte CEA-CNRS-UVSQ, CEA Saclay, 91191 Gif-sur-Yvette, France.

92 |

93 | Abstract.

94 | The Infrared Atmospheric Sounding Interferometer (IASI) is a spaceborne passive sensor of
95 | new generation mainly dedicated to meteorological applications. Operational Level-2
96 | products are available via the European Organisation for the Exploitation of Meteorological
97 | Satellites (EUMETSAT) since several years. In particular, vertical profiles of water vapor
98 | measurements are retrieved from infrared radiances at the global scale. Nevertheless, the
99 | robustness of such products has to be checked because only few validations have been
100 | reported. For this purpose, the field experiments that were held during the HyMeX and
101 | ChArMEx international programs are a very good opportunity. A H₂O-Raman lidar was
102 | deployed on the Balearic Island of Menorca and operated continuously during ~6 and ~3
103 | weeks during fall 2012 (Hydrological cycle in the Mediterranean eXperiment -HyMeX-) and
104 | summer 2013 (Chemistry-Aerosol Mediterranean Experiment -ChArMEx-), respectively. It
105 | measured simultaneously the water vapor mixing ratio and aerosol optical properties. This
106 | article does not aim to describe the IASI operational H₂O inversion algorithm, but to compare
107 | the vertical profiles derived from IASI onboard MetOp-A and the ground-based lidar
108 | measurements to assess the reliability of the IASI operational product for the water vapor
109 | retrieval in both the lower and middle troposphere. The links between water vapor contents
110 | and both the aerosol vertical profiles and the air mass origins are also studied. About 30

111 simultaneous observations, performed during nighttime in cloud free conditions, have been
112 considered. For altitudes ranging from 2 to 7 km, root mean square errors (correlation) of ~0.5
113 g/kg (~0.77) and ~1.1 g/kg (~0.72) are derived between the operational IASI product and the
114 available lidar profiles during HyMeX and ChArMEx, respectively. The values of both root
115 mean square error and correlation are meaningful and show that the operational Level-2
116 product of the IASI-derived vertical water vapor mixing ratio can be considered for
117 meteorological and climatic applications, at least in the frame of field campaigns.

118 1 Introduction

119 Satellite observations are powerful tools for meteorological forecast. Their assimilation in
120 models lead to an improvement on weather forecasts (e.g. *Collard and McNally, 2009;*
121 *Bormann et al., 2010*). Among the main components of the atmospheric state, water vapor is
122 an essential element, which plays a key role in frontogenesis, convection (e.g. *Held and*
123 *Soden, 2000*), cloud formation and aerosol hydration (e.g. *Larson and Taylor, 1983; Rood et*
124 *al., 1987; Randriamiarisoa et al., 2006*). In this way, it influences significantly the Earth
125 climate and the atmospheric chemistry (e.g. IPCC, 2014). It is also an energy reservoir that
126 exchanges with both the atmosphere and the surface through condensation and evaporation
127 processes via the latent heat flux. Hence, for reliable weather forecasts, the vertical profile of
128 the water vapor has to be precisely assessed.

129 During several decades, passive radiometers, such as those implemented onboard of the
130 Television InfraRed Operational Satellite (TIROS) from the National Oceanographic and
131 Atmospheric Administration (NOAA), have allowed to retrieve temperature and moisture
132 profiles with a vertical resolution of about 3 to 5 km in the troposphere, as defined by the
133 instrumental weighting functions (e.g. *Susskind et al., 1984; Chedin et al., 1985*). A new
134 generation of instruments has been launched on polar platforms satellites, such as

135 | Interferometric Monitor for Greenhouse gases (IMG, e.g. Ogawa et al., 1994; Clerbaux et al.,
136 | 1998), Tropospheric Emission Spectrometer (TES, e.g. Shephard et al., 2008; Worden et al.,
137 | 2012), the Advanced Infrared Sounder (AIRS, Chahine et al., 1990; Aumann and Miller,
138 | 1995), and the Infrared Atmospheric Sounding Interferometer (IASI, e.g. Clerbaux et al.,
139 | 2009; Hilton et al., 2012). Thanks to a larger number of spectral channels and an enhanced
140 | spectral resolution, these instruments lead to improved vertical resolutions down to 1 km and
141 | higher precision of both the atmospheric temperature and water vapor content retrieval.

142 | We will focus our study on the reliability of the water vapor mixing ratio (WVMR) vertical
143 | profiles retrieved from the IASI spectrometer, which has been launched onboard the polar
144 | orbiting meteorological satellites MetOp (Meteorological Operational), which forms the space
145 | segment of the overall EUMETSAT Polar System (EPS).

146 | Main mission of IASI is the operational meteorology (e.g. Zhou et al., 2009), although air-
147 | composition and climate applications are also well covered by the instrument as also
148 | discussed before launch (e.g. Chazette et al., 1998; Clerbaux et al., 1998) and now
149 | demonstrated (e.g. Crevoisier et al., 2013a; Griffin et al., 2013; Grieco et al., 2013). Hereafter
150 | we will only discuss the comparison between IASI-derived WVMR and the simultaneous
151 | measurements performed by a H₂O-Raman lidar deployed on the Balearic Island of Menorca
152 | in the frame of the Hydrological cycle in the Mediterranean eXperiment (HyMeX,
153 | <http://www.hymex.org/>, Chazette et al., 2013) and Chemistry-Aerosol Mediterranean
154 | Experiment (ChArMEx, <http://www.mistrals-home.org>).

155 | For our concern, the IASI-derived WVMR operational Level-2 products have been available
156 | via the European Organisation for the Exploitation of Meteorological Satellites
157 | (EUMETSAT) for several years. In particular, vertical profiles of WVMR measurements are
158 | retrieved from infrared radiances at the global scale (e.g. Carissimo et al., 2005; Schlüssel et

159 | *al.*, 2005; *Schneider and Hase*, 2011). The robustness of such products has to be checked, and
160 | the field experiments that were held during the HyMeX and ChArMEx international programs
161 | are a very good opportunity for that purpose. Few validation exercises have been conducted
162 | on the WVMR operational product. The main reason seems that for meteorological
163 | forecasting, the radiances are directly assimilated in the models (e.g. *Hilton et al.*, 2009;
164 | *Hilton et al.*, 2012; *Heilliette*, 2013; *Matricardi and McNally*, 2013; *Xu et al.*, 2013).
165 | Nevertheless, the WVMR Level-2 product could have a great interest in order to help field
166 | experiment analyses. Moreover, few validations are available in the scientific literature.
167 | *Pougatchev et al.* (2009) used rawinsounding measurements to assess the error covariance
168 | matrix needed for the inversion algorithm. *Masiello et al.*, (2013) argue that lidar
169 | measurements are excellent candidates for the validation of spaceborne sensors. They used
170 | different measurement techniques during the Convective and Orographically-induced
171 | Precipitation Study (COPS) campaign, and the comparisons were performed with a limited
172 | number of lidar profiles (6) during the same season. Such validations are very delicate
173 | because performing atmospheric measurements of WVMR with the required accuracy for
174 | satellite retrieval validation is a challenging issue due to the high spatio-temporal variability
175 | of atmospheric water vapor. The spatiotemporal coincidence between the ground-based and
176 | the spaceborne measurements has to be guaranteed to avoid important sampling errors.

177 | In the following section, the Raman lidar system used for IASI WVMR comparisons and its
178 | technical specifications will be presented as well as the experimental sites used to conduct the
179 | validation during the Mediterranean project. The IASI derived WVMR product specifications
180 | will also be introduced. The third section will present the experimental comparisons. The
181 | statistical tools used to evaluate the WVMR products will be introduced and the experimental
182 | results obtained will be presented. Then, the influence of both the air mass origin and their

183 aerosol content in the results will be discussed. Finally, the main results will be recalled in the
184 conclusion.

185 2 Observations

186 | The comparison between the WVMR ground-based lidar measurements and the IASI
187 | operational products took place in the frame of both HyMeX and ChArMEx Special
188 | Observation Periods during September-October 2012 and June-July 2013, respectively, on the
189 | Balearic island of Menorca. During HyMeX/IODA-MED (Innovative Observing and Data
190 | Assimilation systems for the MEDiterranean Weather), the Water vapour and Aerosol lidar
191 | (WALI) was located close to La Ciutadella (Western part of the island, 39°60'00" N and
192 | 3°50'20"E), while during ChArMEx it was deployed close to Mahon (Eastern part of the
193 | island, 39°53'12" N and 4°15'31" E). Hence, the WVMR vertical profiles derived from the
194 | IASI spaceborne spectrometer (Ether CNES/CNRS-INSU Ether web site <http://www.pole-ether.fr>)
195 | have been compared to the ones measured by WALI during nighttime for field
196 | experiment durations of 6 and 3 weeks for HyMeX and ChArMEx, respectively. The use of
197 | the Raman technique limits the range of daytime measurements (< 1 km), which are
198 | consequently not relevant for a validation purpose in the lower and middle troposphere.

199 | 2.1 The WALI Raman lidar

200 | The WALI instrument uses an emitting wavelength of 354.7 nm and is designed to fulfill eye-
201 | safe conditions (Table 1). The instrument, its calibration and the associated errors are
202 | documented in *Chazette et al.* (2013) and will not be detailed here. During all the experiment
203 | the acquisition was performed for mean profiles of 1000 laser shots leading to a temporal
204 | sampling close to 1 minute. The UV pulse energy is ~60 mJ and the pulse repetition
205 | frequency is 20 Hz. It is equipped with four detection channels: an aerosol board including
206 | co-polarized and cross polarized channels with respect to the laser emission, a channel

207 dedicated to the detection of the water vapor Raman signal at 407.5 nm and a fourth channel
208 dedicated to the recording of the atmospheric nitrogen Raman signal at 386.6 nm.

209 The design of the WALI system leads to very good capabilities in terms of low altitude
210 overlap and WVMR retrieval during nighttime. The absolute deviation from rawindsoundings
211 is less than 0.5 g/kg (*Chazette et al.*, 2013). The error on the WVMR reaches 11% in the
212 marine boundary layer and decreases to 7% below 5 km range for a temporal averaging of 20
213 minutes and a vertical resolution of 15 m. Precision can deteriorate very quickly thereafter
214 due to the decreasing Signal to Noise Ratio (SNR) with altitude. It is also worse during
215 daytime, but measurements can be performed with the same uncertainty for altitude ranges
216 below 1 km using a temporal averaging over ~1 hour. For the inter-comparisons presented in
217 this paper, the chosen averaging time is 30 minutes, centered on the time value of the IASI
218 profile to be compared, and the altitude range is from 0.3 to 7 km above the mean sea level
219 (amsl). The original vertical and temporal resolutions are 15 m and 1 minute, respectively.

220 The lidar profiles were smoothed for the comparison so that the vertical resolution used for
221 this study is ~41 m.

222 2.2 The MetOp /IASI satellite data

223 MetOp (Meteorological Operational) consists of a series of three polar heliosynchronous
224 orbiting satellites, to be flown successively for more than 14 years, from 2006. This series
225 forms the space segment of the overall EUMETSAT Polar System (EPS). EPS is the
226 European contribution to the Initial Joint Polar System agreement (IJPS), an agreement
227 between EUMETSAT and NOAA. MetOp flies in a Low Earth orbit at an altitude of 817 km
228 corresponding to local 'morning', while the US is responsible for 'afternoon' coverage (*Klaes
229 et al.*, 2007). MetOp-A (launched on 19 October 2006) and MetOp-B (launched on 17
230 September 2012) provide detailed observations of the global atmosphere, oceans and

231 continents. MetOp-C is due to be launched in 2017. The series provides data for both
232 operational meteorology and climate studies. A combination of passive remote sensing
233 instruments offers the capability to observe the Earth by day and night, as well as under
234 cloudy conditions. The most innovative and one of the key instruments on MetOp is the
235 Michelson interferometer IASI. Three IASI instruments were developed for MetOp by CNES
236 (Centre National d'Etudes Spatiales) in cooperation with EUMETSAT. They are built to
237 provide temperature and moisture measurements with unprecedented accuracy and resolution,
238 and additionally to provide information for the monitoring of atmospheric trace gases.

239 The bandwidth of IASI is divided into 8461 spectral channels between 645 and 2760 cm^{-1} with
240 a mean spectral resolution of 0.5 cm^{-1} after apodization. IASI scans across-track in 30
241 successive elementary fields of view (EFOV), each composed of 4 instantaneous fields of
242 view (IFOV) of 0.8225° leading to a footprint of 12 km diameter at sub-satellite point. The
243 footprint dimension increases from 20 to 39 km along-track directions to the swath edge,
244 respectively (Cayla, 1993). The swath width on the ground is approximately 2200 km, which
245 provides global Earth coverage twice per day.

246 Operational products from EPS/MetOp are generated in the EPS Core Ground Segment. The
247 IASI Level-2 processing development targeted the generation of temperature and humidity
248 profile information, the associated surface information and the retrieval of some trace gas
249 species: CO, O₃, CH₄, N₂O and CO₂. The vertical temperature and water-vapor profiles are
250 currently distributed on a 90-level grid extending between 0.005 and 1050 hPa (August *et al.*,
251 2012). Note that the operational product uses a statistical approach to retrieve the geophysical
252 parameters. Other approaches use a physical scheme and give access to a better vertical
253 resolution (e.g. Amato *et al.*, 2009; Masiello *et al.*, 2013). Nevertheless, the goal of this paper

Mis en forme : Police :Italique

254 | is to provide quantitative elements of validation for the operational product using the
255 | statistical approach.

256 Both the temperature and moisture of the troposphere and lower stratosphere are derived
257 under cloud-free conditions with a vertical resolution of 1-2 km in the lower troposphere; a
258 horizontal resolution of 25 km, and an accuracy of 1 K and 10%, respectively. The number of
259 independent pieces of information which are determined in the moisture profiles is in the
260 order of 10. The sensitivity to the lower troposphere is lower and leads to larger error beneath
261 3 km, although ~80% of moisture is contained in this layer. For the WVMR retrieval, the
262 IASI weighting functions are generally maximum above 700 hPa.

263 For the comparison presented hereafter, we considered the 12 closest IASI pixels from the
264 | lidar ground-based station. The mean values and the associated standard deviations are then
265 | calculated if the number of relevant IASI-derived WVMR profiles are at least equal to 6.

266 3 Comparison between the IASI and WALI water vapor products

267 Here we assess the representativeness of IASI in terms of atmospheric moisture content
268 considering both vertical profiles and integrated values to evaluate the potentiality of these
269 products to be used for meteorological studies purposes. The relevant IASI coincidences are
270 | established before a comparison with the Raman lidar WALI separately for the two time
271 | periods of field experiments.

272 3.1 Coincidences

273 | Figure 1 gives the temporal evolution of the WVMR vertical profiles above Menorca during
274 | the two time periods on which field experiments were conducted. The water vapor contents
275 are highly variable and highlight contrasted atmospheric situations, which are of interest for
276 comparison to IASI-derived WVMR. On the same figure are given the satellite overpass times
277 for which comparisons are relevant. We have identified 30 coincidences in cloud-free

278 conditions with available IASI profiles, during September-October 2012 and June-July 2013.
 279 Note that the presence of high aerosol content is also classified as a cloudy condition. For
 280 each time period, the coincidences are identified by their number in a chronological way
 281 hereafter called coincidence number (CN). All the coincidences are reported in [Table 2](#) and
 282 [Table 3](#) for the time periods of HyMeX and ChArMEx, respectively (15 CN each). The
 283 distance between the central pixel of IASI and the [lidar](#) ground-based station (D), and the
 284 number of relevant IASI pixels (N) are also indicated.

285 3.2 WVMR vertical profiles

286 The WVMR vertical profiles for the whole retained atmospheric situations are shown in
 287 [Figure 2](#) and [Figure 3](#) for HyMeX and ChArMEx, respectively. The coincident WVMR
 288 simulated from the European Centre for Medium-range Weather Forecasts (ECMWF)
 289 operational analysis are also plotted on the figures. The 9 closest model grids from the
 290 ground-based [lidar](#) station are considered to compute both the mean and the standard
 291 deviation vertical profiles. The meteorological fields have been provided by ECMWF and
 292 have been obtained from the ESPRI/IPSL data server for a horizontal resolution of 0.5° .

293 The statistical indicators used to evaluate the relevance of the IASI-derived WVMR (r_{iasi})
 294 with respect to [lidar](#) observations (r_{lidar}) are the Root Mean Square Error (RMSE) and the
 295 (Pearson) correlation (COR). They are often used to evaluate model performances as in
 296 *Boylan and Russell (2006)* and can be written as

$$297 \quad RMSE = \sqrt{\frac{1}{N_t} \sum_{i=1}^{N_t} (r_{iasi} - r_{lidar})^2} \quad (1)$$

$$298 \quad COR = \frac{\sum_{i=1}^{N_t} (r_{lidar} - \bar{r}_{lidar})(r_{iasi} - \bar{r}_{iasi})}{\sqrt{\sum_{i=1}^{N_t} (r_{lidar} - \bar{r}_{lidar})^2 \sum_{i=1}^{N_t} (r_{iasi} - \bar{r}_{iasi})^2}} \quad (2)$$

299 where N_i is the total number of coincidences and the overbar terms are averages. The vertical
300 values for both $\overline{r_{IASI}}$ and $\overline{r_{lidar}}$ are used at the IASI-L2 pressure level grid.

Mis en forme : Police :Italique

Mis en forme : Police :Italique, Indice

Mis en forme : Police :Italique

301 Figure 4 gives the vertical profiles of both RMSE and COR for the two time periods. The
302 statistical indicators have been computed between WALI and IASI, and WALI and ECMWF
303 data.

304 During the first time period (fall time), the lidar and modelled profiles are in better agreement
305 with a mean RMSE and COR of 0.42 g/kg and 77% (between 0.5 and 7 km), respectively,
306 whereas between the lidar and IASI vertical profiles these values reach ~0.6 g/kg and 70%,
307 respectively. The shapes of RMSE and COR against altitude are however very similar. It is
308 not surprising because ECMWF analyses are made by assimilating the IASI radiances (e.g.
309 Hilton *et al.*, 2012) in addition to the rawinsounding performed in Palma de Mallorca (100 km
310 Southwest of Menorca). In the planetary boundary layer (PBL) more discrepancy could be
311 encountered due to local effects.

312 An opposite behavior happens in terms of RMSE for the second time period (summer time)
313 where the IASI-derived WVMR ($RMSE = 1.64$ g/kg) is better than that of the model
314 ($RMSE = 2.04$ g/kg) when compared to the Raman lidar. It is mainly true below 2 km.
315 Nevertheless, the correlation is better between the lidar and the ECMWF analyses (0.82) than
316 between the lidar and IASI (0.59).

317 In the free troposphere, where the IASI weighted functions mostly have their maxima, the
318 agreement is better according to the two indicators that are the COR and RMSE indicators.
319 This agreement is higher for the HyMeX time period and might be due to a lesser influence of
320 the aerosol layers. For this period $RMSE$ is lower than 0.5 g/kg and COR is ~77%, to be
321 compared to ~1.1 g/kg and ~72% during the ChArMEx time periods. Below 2 km, the
322 agreement is degraded as expected: $RMSE$ is between ~2 and 3 g/kg and the COR value tends

323 to 0. Table 4 summarizes the results for different atmospheric layers between 0.5 and 7 km.
324 Such results are consistent with those of *Schneider and Hase* (2011) who used
325 rawinsoundings as validation tools for the IASI WVMR Level-2 operational products. With
326 the exception of the PBL, they found a correlation coefficient of ~ 0.80 .

327 3.3 Water vapor integrated content

328 When considering the Water vapor integrated content (WVIC) between 0.5 and 7 km, the
329 agreement between lidar- and IASI-derived moisture is within a standard deviation between
330 0.18 and 0.25 g/cm². **Figure 5** illustrates this agreement: the IASI-derived WVIC exhibits a
331 bias lower than 0.15 g/cm² compared to the one retrieved from WALI. In fact, the WVIC
332 retrieved from IASI is in the range value (between 0.5 and 2 g/cm²) for the HyMeX time
333 period (fall 2012), but it is mostly underestimated by $\sim 10\%$ during the ChArMEx time period
334 (summer 2013). The slopes of the regressions are 0.89 and 0.81 for the HyMeX and
335 ChArMEx time periods, respectively. Note that during the HyMeX time period (fall 2012),
336 the agreement between the lidar and IASI profiles is better, even in the general shape.

337 When compared to ECMWF analyses, standard deviations with respect to WALI are close to
338 0.17 and 0.45 g/cm² for the two previous time periods, respectively. With respect to previous
339 IASI cross-comparisons, results are not degraded during the HyMeX fall period but
340 significantly worse over the ChArMEx summer period where the slope of the linear fit is
341 close to 0.70. Such discrepancy (underestimation) may be due to an incorrect consideration of
342 the instrumental error in the variance/covariance matrix needed for the assimilation process
343 (e.g. *Wang et al.*, 2013). The error on the contribution to the IASI radiances may be linked to
344 local heating associated to the aerosol presence not being taken into account in the model, as
345 for all spaceborne infrared sensors (e.g. *Pierangélo et al.*, 2004). This point is not within the
346 topic of this paper and has to be further investigated.

347 4 Influence of the air mass origins - aerosol as air mass tracer

348 Among all 30 coincidences, the origins of air masses are very different and can be
349 characterized using simultaneously several aerosol optical properties and air mass back
350 trajectories. The Raman lidar WALI offers the capability to retrieve fundamental aerosol
351 optical properties (Chazette *et al.*, 2013): the vertical profiles of the volume depolarization
352 ratio (VDR) to identify the presence of dust-like aerosols, the aerosol extinction coefficient
353 (AE) to locate in altitude the scattering layers, the equivalent backscatter to extinction ratio
354 (BER) which is proportional to the single scattering albedo, and the aerosol optical thickness
355 (AOT) characterizing the aerosol column burden. The inversion process used both the N₂-
356 Raman and elastic channels at 355 nm and is described in various papers as Royer *et al.*
357 (2011) or Chazette *et al.* (2012) where the related uncertainties are assessed. Hence, using the
358 aerosol optical properties described above, coupled with air mass back trajectory analysis, the
359 air masses influencing the IASI-derived WVMR can be identified.

360 4.1 Aerosol optical properties

361 As in Figure 1, the dates of the relevant IASI coincidences are highlighted in white dotted
362 lines in Figure 6. This figure represents the temporal evolution of the vertical profile of VDR
363 for HyMeX and ChArMEX time periods, respectively. In general, the relevant coincidences do
364 not occur during the major dust events where the VDR is maximal (in brown on the figure),
365 likely because the dust plume is classified as cloud: it is sufficiently thick to significantly
366 influence the brightness temperature used to inverse the IASI infrared spectrum. Nevertheless,
367 other sources of aerosol may affect the IASI measurements. Thereby, the BER is also an
368 important parameter to identify the aerosol types (e.g. Catrall *et al.*, 2005) as it is linked to
369 their chemical composition. It is given in Figure 7 as a column average and presents a strong
370 variability, ranging from $\sim 0.01 \text{ sr}^{-1}$ for pollution aerosol (e.g. Raut and Chazette, 2009) to
371 $\sim 0.04 \text{ sr}^{-1}$ for marine aerosol (e.g. Flamant *et al.*, 2000). The intermediate values are for

372 aerosol mixing, dust aerosols (e.g. *Mattis et al.*, 2002; *Chazette et al.*, 2007) or long-range
373 transport pollution aerosols (e.g. *Chazette et al.*, 2012). The AE and VDR vertical profiles are
374 also given [Figure 8](#) and [Figure 9](#) for the coincidences of the two time periods. They often
375 show strong heterogeneities with respect to altitude which are directly related to the vertical
376 profiles of WVMR given [Figure 2](#) and [Figure 3](#), respectively. All the vertical structures
377 encountered have to be investigated to compare the WVMR-derived from IASI and WALI.
378 The aerosol atmospheric content in terms of AOT is also very different from one observation
379 to another because it ranges from 0.04 (very clean air) to ~0.4 (polluted air and/or dust event).
380 Hence, the coincidences are very diverse for an inter-comparison exercise, and allow
381 evaluating the IASI-derived WVMR retrieval for very distinct atmospheric situations and
382 aerosol contents.

383 4.2 Air mass back trajectories

384 Air mass back trajectories have been computed to determine the corresponding aerosol
385 transport routes using the NOAA Hybrid Single Particle Lagrangian Integrated Trajectory
386 (HYSPLIT) model (*Draxler and Rolph*, 2003) with 3-hourly archived meteorological data
387 provided from the US National Centers for Environmental Prediction (NCEP) Global Data
388 Assimilation System (GDAS) at the horizontal resolution of 0.5° . The altitudes of the
389 trajectory starting points (1, 2 and 4 km) were selected primarily from the [lidar](#) observations
390 of aerosol layer heights highlighted in [Figure 8](#) and [Figure 9](#). The air mass back trajectories
391 are shown [Figure 10](#), [Figure 11](#) and [Figure 12](#) for the 3 starting points and for each time
392 period. One path was drawn on 72 hours for each coincidence between IASI and WALI
393 measurements. The air mass origins are very variable during the time periods for all starting
394 point altitudes. There are two major contributions to the air masses passing over Menorca, the
395 first one from the Sahara and the second one from the Atlantic Ocean.

396 4.3 Discussion

397 The summary of our conclusion about the origins of air mass revealed by the shape of the
398 WVMR vertical profile is given in [Table 2](#) and [Table 3](#) for the HyMeX and ChArMEx time
399 periods, respectively. Depolarizing layers (DL) and residual pollution layers (RPL) are
400 specifically identified.

401 The atmospheric situations observed during the coincidences present significantly high
402 moisture content ($WVMR > 5 \text{ g/kg}$ in the free troposphere and $WVIC$ close to 2 g/cm^2) for 4
403 (5) cases during the HyMeX (ChArMEx) time period, which correspond to $CN = 1, 2, 6$ and
404 10 (2, 5, 6, 7 and 8). Such situations are generally well represented by the Level-2 product of
405 the IASI operational ground segment, excepted for $CN = 10$ during the HyMeX time period
406 where the IASI product overestimates the WVMR by $\sim 25\%$. In this case, the air mass came
407 from Morocco and brought moisture with dust aerosols between ground and $\sim 4 \text{ km}$ above the
408 mean sea level (amsl). Nevertheless, it must be noted that Saharan air masses are often
409 associated with higher moisture content and the agreement between IASI- and WALI-derived
410 WVMR is generally better for these air masses because of the smoother transitions in vertical
411 structures due to higher moisture content in these layers.

412 The major discrepancies are observed for the drier air masses ($WVIC$ less or close to 1 g/cm^2)
413 which present a strong vertical gradient of WVMR, generally between the PBL and the free
414 troposphere. Such a gradient is not reproduced from IASI measurements due to its insufficient
415 vertical resolution. Note that the dry air masses observed during the field campaigns
416 originated from the Atlantic and had a small AOT (< 0.2).

417 For the other coincidences, the agreement between IASI and WALI is good. The median
418 value of the atmospheric aerosol content ($AOT \sim 0.2$) is similar during the two time periods
419 and cannot explain the observed differences between them. During the ChArMEx time period

420 several coincidences are associated with very clean air ($AOT < 0.1$) situations. Furthermore,
421 the differences observed in the WALI/ECMWF comparison cannot be explained by the
422 presence of an aerosol layer. These discrepancies seem linked to a seasonal role, which could
423 be due to an incorrect consideration of the sea surface temperature in the model.

424 The air mass origin plays a major role through the shape of the original vertical structure
425 which can be kept during several days along the transport. As discussed by *Kim et al.* (2004),
426 the larger amount of water vapor in an aerosol layer contributes to a higher radiative heating,
427 increasing the potential temperature and static stability of the layer. This may help to maintain
428 the structure of the layer for a longer period of time. Note that the vertical structures observed
429 during our two field campaigns are not uncommon in the atmosphere (e.g. *Chazette et al.*,
430 2001; *Kim et al.*, 2009). All this suggests a need for an increased vertical resolution of
431 infrared spaceborne sounders, and then for the improvement of their spectral resolution (e.g.
432 *Crevoisier et al.*, 2013b).

433 5 Conclusion

434 Following the international field campaigns HyMeX and ChArMEx in fall 2012 and summer
435 | 2013, respectively, 30 relevant coincidences between the ground-based lidar WALI and the
436 | spaceborne instrument IASI have been selected to conduct a comparison exercise of the
437 WVMR vertical profile retrieval. The general result is in good agreement between the two
438 instruments. Two statistical indicators generally used to evaluate model performances have
439 been considered: the Root Mean Square Error (RMSE) and the (Pearson) correlation (COR).
440 In the middle troposphere (2-7 km amsl) the COR value is ~77 and 72%, and the RMSE is
441 lower than 0.5 and 1.1 g/kg for the fall and summer periods, respectively. Discrepancies are
442 higher in the PBL because the weighted functions of IASI do not correctly sample this layer
443 close to the ground ($RMSE \sim 1.6$ g/kg and $COR < 0.4$). Considering the water vapor integrated

444 content within the altitude range of 0.3 and 7 km amsl, the standard deviation between IASI
445 and WALI are 0.18 and 0.25 g/cm² for the fall and summer periods, respectively. The
446 disagreement is higher during summer time and we may suspect the presence of aerosol layers
447 and/or contrasted vertical atmospheric structures to be responsible for this bias.

448 During coincidences, we note that the integrated atmospheric aerosol content has been found
449 with aerosol optical thickness between 0.04 and 0.4 associated with various particle types
450 (pollution, marine or dust aerosols), as identified from both the lidar-derived backscatter to
451 extinction ratio and air mass back trajectories. The aerosol optical thickness does not
452 significantly affect the results of the intercomparison. The divergence on the WVMR vertical
453 profile is mainly due to the existence of sharp transitions which mainly occurs between the
454 PBL and the free troposphere. The agreement is generally better for Saharan air masses
455 because of the smoother transitions in vertical structures due to higher moisture content in
456 these layers (~5 g/kg). Our results calls for an improvement of the spectral resolution of the
457 Fourier transform spectrometer IASI. Such consideration is being studied for the next
458 generation, the so-called IASI-NG. Moreover, the synergetic use of microwave measurements
459 is capable of improving the water vapor retrievals, especially in the PBL. An upcoming
460 version (6) of the operational IASI Level 2 processor with synergistic use of the Advanced
461 Microwave Sounding Unit (AMSU) and the Microwave Humidity Sounder (MHS) data is
462 scheduled. It was reported to contain substantial improvements of the profiles when compared
463 with ECMWF analysis, in particular in the lower levels and for the entire water vapor profiles.
464 The approach presented in this study can be applied to the next generation of IASI operational
465 water vapor products.

466 **Acknowledgments.** This work was supported by the French Agence Nationale de la
467 Recherche (ANR) via the HyMeX /IODA-MED project, the French space agency (CNES) and

468 the Commissariat à l'Energie Atomique (CEA). We also thank M. Sicard and F. Dulac for
469 their help for installing the **lidar** station on the Menorca Island. ECMWF data used in this
470 study have been obtained from the ECMWF Data Server. The authors would additionally like
471 to thank the HyMeX and ChArMEx programs for their support. The IASI Level-2 Water
472 Vapor Mixing Ratio profiles used in this paper are Courtesy Ether CNES/CNRS-INSU Ether
473 web site <http://www.pole-ether.fr>.

474

475 6 References

- 476 Amato, U., Antoniadis, A., De Feis, I., Masiello, G., Matricardi, M., and Serio, C.: Technical
477 Note: Functional sliced inverse regression to infer temperature, water vapour and ozone
478 from IASI data, *Atmos. Chem. Phys.*, 9, 5321-5330, doi:10.5194/acp-9-5321-2009, 2009.
- 479 Aumann, H.H., and Miller, C.: Atmospheric Infrared Sounder (AIRS) on the Earth Observing
480 System, in *Advanced and next-generation satellite*, H. Fujisada and M.N. Sweeting, eds.,
481 Proc. SPIE 2583, 332-338, 1995.
- 482 August, T., Klaes, D., Schlüssel, P., Hultberg, T., Crapeau, M., Arriaga, A., O'Carroll, A.,
483 Coppens, D., Munro, R., and Calbet, X.: IASI on Metop-A:Operational Level 2 retrievals
484 after five years in orbit, *Journal of Quantitative Spectroscopy & Radiative Transfer*, 113,
485 1340–1371, 2012.
- 486 Bormann, N., Collard, A., and Bauer, P.: Estimates of spatial and interchannel observation-
487 error characteristics for current sounder radiances for numerical weather prediction. II:
488 Application to AIRS and IASI data, *Q. J. Roy. Meteorol. Soc.*, 136, 1051-1063, 2010.
- 489 Boylan, J. W. and Russell, A. G.: PM and light extinction model performance metrics, goals,
490 and criteria for three-dimensional air quality models, *Atmos. Environ.*, 40, 4946–4959,
491 2006.
- 492 Carissimo, A., De Feisi, I., and Serio, C.: The physical retrieval methodology for IASI: the -
493 IASI code, *Environ. Modell. Softw.*, 20, 9, 1111–1126, doi:10.1016/j.envsoft.2004.07.003,
494 2005.
- 495 | Cattrall, C., Reagan, J., Thome, K., and Dubovik, O.: Variability of aerosol and spectral **lidar**
496 and backscatter and extinction ratios of key aerosol types derived from selected Aerosol
497 Robotic Network locations, *J. Geophys. Res.*, 110, D10S11, doi:10.1029/2004JD005124,
498 2005.
- 499 Cayla, F-R.: IASI infrared interferometer for operations and research. In: Chedin A, Chahine
500 MT, Scott NA, editors. High spectral resolution infrared remote sensing for Earth's
501 weather and climate studies, NATO ASI series, vol. I 9. Berlin: Springer Verlag, 1993.
- 502 Chahine, M.T., O'Callaghan, F.G., Aumann, H.H., Capps, R.W., Haskins, R.D., Pagano, R.J.,
503 and Schlindler, R.A.: Atmospheric Infrared Sounder (AIRS)-Science and measurement
504 requirements, NASA-TM-104977, Washington D.C., 36 pp, 1990.
- 505 Chazette, P., Clerbaux, C., and Mégie, G.: Radiative forcing of methane estimated using nadir
506 spectral radiances, *Appl. Opt.*, 37, 15, 3113-3120, 1998.
- 507 Chazette, P., Pelon, J., Moulin, C., Dulac, F., Carrasco, I., Guelle, W., Bousquet, P., and
508 | Flamant, P.H.: Airborne **lidar** and Meteosat synergy to characterize a Saharan dust plume
509 over the Azores during SOFIA/ASTEX, *Atmos. Environ.*, 35, 4297-4304, 2001.

- 510 | Chazette, P., Sanak, J., and Dulac, F.: New Approach for Aerosol Profiling with a **lidar**
511 | Onboard an Ultralight Aircraft: Application to the African Monsoon Multidisciplinary
512 | Analysis, *Environ. Sci. Technol.*, *41*, 8335–8341, 2007.
- 513 | Chazette, P., Bocquet, M., Royer, P., Winiarek, V., Raut, J.-C., Labazuy, P., Gouhier,
514 | M., Lardier, M., and Cariou, J.-P.: Eyjafjallajökull ash concentrations derived from both
515 | **lidar** and modeling, *J. Geophys. Res.*, *117*, D00U14, doi:10.1029/2011JD015755, 2012.
- 516 | Chazette, P., Marnas, F., and Totems, J.: The mobile Water vapor Aerosol Raman **lidar** and
517 | its implication in the frame of the HyMeX and ChArMEx programs: application to a dust
518 | transport process, *Atmos. Meas. Tech. Discuss.*, *6*, 10653-10698, doi:10.5194/amtd-6-
519 | 10653-2013, 2013.
- 520 | Chedin, A., Scott, N. A., Wahiche, C., and Moulinier, P.: The improved initialization
521 | inversion method: a high resolution physical method fo temperature retrievals from
522 | satellites of the TIROS-N series, *J. Climate Appl. Meteorol.*, *24*, doi:10.1175/1520-
523 | 0450(1985)024, 128:143, 1985.
- 524 | Clerbaux, C., Chazette, P., Hadji-Lazaro, J., Müller, J.F., Clough, T., and Mégie, G.: Remote
525 | sensing of O₃, CO and CH₄ using a spaceborne nadir-viewing instrument, *J. Geophys. Res.*,
526 | *103*, D15, 18999-19013, 1998.
- 527 | Clerbaux, C., Boynard, A., Clarisse, L., George, M., Hadji-Lazaro, J., Herbin, H., Hurtmans,
528 | D., Pommier, M., Razavi, A., Turquety, S., Wespes, C., and Coheur, P.-F.: Monitoring of
529 | atmospheric composition using the thermal infrared IASI/MetOp sounder, *Atmos. Chem.*
530 | *Phys.*, *9*, 6041–6054, doi:10.5194/acp-9-6041-2009, 2009.
- 531 | Collard, A.D., and McNally, A.P.: The assimilation of Infrared Atmospheric Sounding
532 | Interferometer radiances at ECMWF, *Q. J. Roy. Meteorol. Soc.*, *135*, 1044-1058, 2009.
- 533 | Crevoisier, C., Nobileau, D., Armante, R., Crépeau, L., Machida, T., Sawa, Y., Matsueda, H.,
534 | Schuck, T., Thonat, T., Pernin, J., Scott, N. A., and Chédin, A.: The 2007–2011 evolution
535 | of tropical methane in the mid-troposphere as seen from space by MetOp-A/IASI, *Atmos.*
536 | *Chem. Phys.*, *13*, 4279-4289, doi:10.5194/acp-13-4279-2013, 2013a.
- 537 | Crevoisier, C., Clerbaux, C., Guidard, V., Phulpin, T., Armante, R., Barret, B., Camy-
538 | Peyret, C., Chaboureaud, J.-P., Coheur, P.-F., Crépeau, L., Dufour, G., Labonnote, L.,
539 | Lavanant, L., Hadji-Lazaro, J., Herbin, H., Jacquinet-Husson, N., Payan, S., Péquignot, E.,
540 | Pierangelo, C., Sellitto, P., and Stubenrauch, C.: Towards IASI-New Generation (IASI-
541 | NG): impact of improved spectral resolution and radiometric noise on the retrieval of
542 | thermodynamic, chemistry and climate variables, *Atmos. Meas. Tech. Discuss.*, *6*, 11215-
543 | 11277, doi:10.5194/amtd-6-11215-2013, 2013b.
- 544 | Draxler, R.R., and Rolph, G.D.: HYSPLIT (HYbrid Single-Particle Lagrangian Integrated
545 | Trajectory) Model access via NOAA ARL READY Website

546 (<http://www.arl.noaa.gov/ready/hysplit4.html>). NOAA Air Resources Laboratory, Silver
547 Spring, MD, 2003.

548 Flamant C., Pelon, J., Chazette, P., Trouillet, V., Quinn, P., Frouin, R., Bruneau, D., Léon,
549 J.F., Bates, T., Johnson, J., and Livingston, J.: Airborne lidar measurements of aerosol
550 spatial distribution and optical properties over the Atlantic Ocean during an European
551 pollution outbreak of ACE-2, *Tellus*, 52B, 662-667, 2000.

552 Grieco, G., Masiello, G., Matricardi, M., and Serio, C.: Partially scanned interferogram
553 methodology applied to IASI for the retrieval of CO, CO₂, CH₄ and N₂O, *Opt. Express*,
554 21, 24753-24769; doi: 10.1364/OE.21.024753, 2013.

555 Griffin, D., Walker, K. A., Franklin, J. E., Parrington, M., Whaley, C., Hopper, J.,
556 Drummond, J. R., Palmer, P. I., Strong, K., Duck, T. J., Abboud, I., Bernath, P. F.,
557 Clerbaux, C., Coheur, P.-F., Curry, K. R., Dan, L., Hyer, E., Kliever, J., Lesins, G.,
558 Maurice, M., Saha, A., Tereszchuk, K., and Weaver, D.: Investigation of CO, C₂H₆ and
559 aerosols in a boreal fire plume over eastern Canada during BORTAS 2011 using ground-
560 and satellite-based observations and model simulations, *Atmos. Chem. Phys.*, 13, 10227-
561 10241, doi:10.5194/acp-13-10227-2013, 2013.

562 Heilliette S., Y. J. Rochon, L. Garand, and J. W. Kaminski: Assimilation of Infrared
563 Radiances in the Context of Observing System Simulation Experiments
564 *Journal of Applied Meteorology and Climatology*, 52(4), 1031-1045, doi:10.1175/JAMC-
565 D-12-0124.1, 2013.

566 Held, I.M., and Soden, B.J.: Water vapor feedback and global warming, *Annual Rev. Energy*
567 *Environ.*, 25, 441-475, DOI: 10.1146/annurev.energy.25.1.441, 2000.

568 Hilton, F., Atkinson, N.C., English, S.J., and Eyre, J.R.: Assimilation of IASI at the Met
569 Office and assessment of its impact through observing system experiments, *Q. J. Roy.*
570 *Meteorol. Soc.*, 135, 495-505, 2009.

571 Hilton, F., Armante, R., August, T., Barnet, C., Bouchard, A., Camy-Peyret, C., Capelle, V.,
572 Clarisse, L., Clerbaux, C., Coheur, P.-F., Collard, A., Crevoisier, C., Dufour, G., Edwards,
573 D., Faijan, F., Fourrié, N., Gambacorta, A., Goldberg, M., Guidard, V., Hurtmans, D.,
574 Illingworth, S., Jacquinet-Husson, N., Kerzenmacher, T., Klaes, D., Lavanant, L.,
575 Masiello, G., Matricardi, M., McNally, A., Newman, S., Pavelin, E., Payan, S., Péquignot,
576 E., Peyridieu, S., Phulpin, T., Remedios, J., Schlüssel, P., Serio, C., Strow, L.,
577 Stubenrauch, C., Taylor, J., Tobin, D., Wolf, W., and Zhou, D.: Hyperspectral Earth
578 Observation from IASI: Five Years of Accomplishments, *Bull. Am. Meteorol. Soc.*, 93,
579 347-370, DOI: 10.1175/BAMS-D-11-00027.1, 2012.

580 IPCC: Climate Change 2013: The physical science basis. Contribution of working group I to
581 the fifth assessment report of the Intergovernmental Panel on Climate Change [Stocker,
582 T.F., D. Qin, G.-K. Plattner, M. Tignor, S.K. Allen, J. Boschung, A. Nauels, Y. Xia, V.

- 583 Bex and P.M. Midgley (eds.]. Cambridge University Press, Cambridge, United Kingdom
584 and New York, NY, USA, 1535 pp., 2013.
- 585 Kim, S-W., Yoon, S-C., Jefferson, A., Won, J-G., Dutton, E.G., Ogren, J.A., and Anderson,
586 T.L.: Observation of enhanced water vapor in Asian dust layer and its effect on
587 atmospheric radiative heating rates, *Geophys. Res. Letters*, 31, L18113,
588 doi:10.1029/2004GL020024, 2004.
- 589 Kim, S.-W., Chazette, P., Dulac, F., Sanak, J., Johnson, B., and Yoon, S.-C.: Transport and
590 vertical structure of aerosols and water vapor over West Africa during the African
591 monsoon dry season, *Atmos. Chem. Phys.*, 9, 8017-8038, 2009.
- 592 Klaes, K.D., Cohen, M., Buhler, Y., Schussel, P., Munro, R., von Engel, A., Clérigh, E.,
593 Bonekamp, H, Ackermann, J., and Schmetz, J.: An introduction to the EUMETSAT polar
594 system, *Bull. Am. Meteorol. Soc.*, 88, 1085–96, doi:10.1175/BAMS-88-7-1085, 2007.
- 595 Larson, T.V., and Taylor, G.S.: On the evaporation of NH₄NO₃ aerosol, *Atmos. Environ.*, 17,
596 2489-2595, 1983.
- 597 Masiello, G., Serio, C., Deleporte, T., Herbin, H., Di Girolamo, P., Champollion, C.,
598 Behrendt, A., Bosser, P., Bock, O., Wulfmeyer, V., Pommier, M., and Flamant, C.:
599 Comparison of IASI water vapour products over complex terrain with COPS campaign
600 data, *Meteorologische Zeitschrift*, 22, 4, 471-487, doi:10.1127/0941-2948/2013/0430,
601 2013.
- 602 Matricardi, M., and McNally, A. P.: The direct assimilation of principal components of IASI
603 spectra in the ECMWF 4D-Var, *Q. J. Roy. Meteor. Soc.*, 140, 573-582,
604 doi:10.1002/qj.2156, 2013.
- 605 Mattis, I., Ansmann A., Müller D., Wandinger U., and Althausen D., Dual-wavelength Raman
606 lidar observations of the extinction-to-backscatter ratio of Saharan dust, *Geophys. Res.*
607 *Let.*, 29, 9, 1306, doi:10.1029/2002GL014721, 2002.
- 608 Ogawa, T., Shimoda, H., Hayashi, M., Imasu, R, Ono, A, Nishinomiya, S, and Kobayashi, H:
609 IMG, Interferometric measurement of greenhouse gases from space, *Adv. Space. Res.*, 14,
610 25-28, 1994.
- 611 Pierangélo, C., Chedin, A., and Chazette, P.: Measurements of Stratospheric Volcanic Aerosol
612 Optical Depth from NOAA/TOVS Observations, *J. Geophys. Res.*, 109, D03207, 2004.
- 613 Pougatchev, N., August, T., Calbet, X., Hultberg, T., Oduleye, O., Schlüssel, P., Stiller, B.,
614 Germain, K. St., and Bingham, G.: IASI temperature and water vapor retrievals – error
615 assessment and validation, *Atmos. Chem. Phys.*, 9, 6453-6458, doi:10.5194/acp-9-6453-
616 2009, 2009.

Mis en forme : Police :Italique

Mis en forme : Police :Italique

- 617 Randriamiarisoa, H., Chazette, P., Couvert, P., and Sanak, J.: Relative humidity impact on
618 aerosol parameters in a Paris suburban area, *Atmos. Chem. Phys.*, *6*, 1389–1407,
619 doi:10.5194/acp-6-1389-2006, 2006.
- 620 | Raut, J.-C., and Chazette, P.: Assessment of vertically-resolved PM₁₀ from mobile **lidar**
621 observations, *Atmos. Chem. Phys.*, *9*, 8617-8638, doi:10.5194/acp-9-8617-2009, 2009.
- 622 Rood, M.J., Covert, D.S., and Larson, T.V.: Hygroscopic properties of atmospheric aerosol in
623 Riverside, California, *Tellus*, *39B*, 383-397, 1987.
- 624 Royer, P., Chazette, P., Lardier, M., and Sauvage, L.: Aerosol content survey by mini-N2-
625 | Raman **lidar**: Application to local and long-range transport aerosols, *Atmos. Environ.*,
626 doi:10.1016/j.atmosenv.2010.11.001, 2011.
- 627 Schneider, M., and Hase, F.: Optimal estimation of tropospheric H₂O and δD with
628 IASI/METOP, *Atmos. Chem. Phys.*, *11*, 11207-11220, doi:10.5194/acp-11-11207-2011,
629 2011.
- 630 Schlüssel, P., Hultberg, T., Phillips, P., August, T. and Calbet, X.: The operational IASI Level
631 2 processor, *Adv. Space Res.*, *36*, 982-988, 2005.
- 632 Shephard, M.W., Herman, R.L., Fisher, B.M., Cady-Pereira, K.E., Clough, S.A., Payne, V.H.,
633 Whiteman, D.N., Comer, J.P., Vömel, H., Miloshevich, L.M., Forno, R., Adam, M.,
634 Osterman, G.B., Eldering, A., Worden, J.R., Brown, L.R., Worden, H.M., Kulawik, S.S.,
635 Rider, D.M., Goldman, A., Beer, R., Bowman, K.W., Rodgers, C.D., Luo, M., Rinsland,
636 C.P., Lampel, M., and Gunson, M.R.: Comparison of Tropospheric Emission Spectrometer
637 Nadir Water Vapor Retrievals with *In Situ* Measurements, *J. Geophys. Res.*, *113*, D15S24,
638 doi:10.1029/2007JD008822, May 16, 2008.
- 639 Susskind, J., Rosenfield, J., Reuter, D., and Chahine, M.T.: Remote sensing of weather and
640 climate parameters from HIRS2/MSU on TIROS-N. *J. Geophys. Res.*, *89*, 4677-4697,
641 1984.
- 642 | Wang, Y., Sartelet, K. N., Bocquet, M., and Chazette, P.: Modelling and assimilation of **lidar**
643 signals over Greater Paris during the MEGAPOLI summer campaign, *Atmos. Chem. Phys.*
644 *Discuss.*, *13*, 27115-27161, doi:10.5194/acpd-13-27115-2013, 2013.
- 645 Worden, J., Kulawik, S., Frankenberg, C., Payne, V., Bowman, K., Cady-Peirara, K.,
646 Wecht, K., Lee, J.-E., and Noone, D.: Profiles of CH₄, HDO, H₂O, and N₂O with improved
647 lower tropospheric vertical resolution from Aura TES radiances, *Atmos. Meas. Tech.*, *5*,
648 397-411, doi:10.5194/amt-5-397-2012, 2012.
- 649 Xu, D., Liu Z., Zhiquan, Huang, X.-Y., Min, J., and Wang, H.: Impact of assimilating IASI
650 radiance observations on forecasts of two tropical cyclones, *Meteorology and Atmospheric*
651 *Physics*, *122*, 1-18, doi: 10.1007/s00703-013-0276-2, 2013.

652 Zhou, D. K., Smith, W. L., Larar, A. M., Liu, X., Taylor, J. P., Schlüssel, P., Strow, L. L., and
653 Mango, S. A.: All weather IASI single field-of-view retrievals: case study – validation with
654 JAIVEx data, *Atmos. Chem. Phys.*, 9, 2241-2255, doi:10.5194/acp-9-2241-2009, 2009.

655

656

657 Table 1: Main technical characteristics of the WALI instrument.

Laser	Nd:Yag
Energy	60 mJ at 355 nm
Frequency	20 Hz
Reception channels	Elastic total 354.67 nm Elastic \perp 354.67 nm Raman-N ₂ 386.63 nm Raman-H ₂ O 407.5 nm
Reception diameters	15 cm
Field of view	~2.3 mrad
Full overlap	~300 m
Detector	Photomultiplier tubes
Filter bandwidths	0.2 - 0.3 nm
Vertical sampling	0.75 m (analog) 15 m (photon counting)
Vertical resolution used for this study	~ 40 m
Acquisition system	PXI technology at 200 MHz

Mis en forme : Anglais (États Unis)

658

659 Table 2: List of the coincidence numbers (CN) and description of the associated aerosol layer
660 synoptic origin during the HyMeX experiment (2012 fall period). *D* represents the distance
661 between the ground-based lidar and the center of the 12 selected IASI pixels. *N* is the number
662 of available averaged IASI profiles. The wettest (driest) coincidences are in bold (italic). The
663 presences of dry layer (DL) and residual particle layer (RPL) are indicated.

(CN) Month/Day - LT	<i>D</i> (km)	<i>N</i>	Observation
(1) 09/19 - 23:03	0.6	8	Atlantic-Spain origin, RPL below 2 km DL between 3 and 4 km, air mass off Eastern African coast
(2) 09/20 - 22:42	2.4	12	Atlantic - Spain origin DL between 2 and 4 km, air mass along Eastern African coast Subsidence between ~0 and 3 km above Southern Spain
(3) 09/22 - 21:59	19.3	12	Saharan origin between 1 and 5 km (Algeria-Morocco) DL between 1 and 4 km, air mass along Eastern African coast Strong ascent from ~0 to 3 km above Morocco
(4) 09/24 - 22:59	2.8	6	Atlantic - Spain origin with a RPL below 1.5 km (from Valencia) Strong subsidence from ~4 to 0 km
(5) 09/25 - 22:39	3.9	12	Atlantic-Southern Spain origin Below 1 km, RPL from Gibraltar with strong subsidence from ~3 km
(6) 09/30 - 22:33	55.2	6	Between 2 and 5 km, Saharan, France and Spain origin Below 1 km, RPL from Gibraltar (petrochemistry) Strong subsidence from 8 to 4 km above Moroccan sea coast
(7) 10/01 - 22:15	8.3	11	Northern Spain - Southwestern France origin RPL below 3 km from Valencia-Barcelona
(8) 10/03 - 23:12	5.2	12	Spain origin RPL below 2 km from Valencia coast
(9) 10/04 - 22:51	2.6	12	Saharan (Morocco) and Southern - Spain origin DL between 2 and 4 km
(10) 10/08 - 23:09	2.1	9	Tropical Atlantic - Spain origin DL below 4 km, mainly between 2 and 4 km May be Saharan air masses off African west coast
(11) 10/09 - 22:48	6.5	12	Tropical Atlantic - Spain origin Below 2 km, RPL from Valencia-Barcelona coast
(12) 10/13 - 23:06	8.5	11	Atlantic - Northern Spain origin RPL from Barcelona coast
(13) 10/16 - 22:03	45.8	6	Atlantic-Spain origin Strong subsidence from 4 to 1 km over Spain RPL from Valencia-Barcelona coast
(14) 10/17 - 23:24	5.2	11	Saharan origin with a strong DL below 3 km Strong subsidence from 4 to 0 km over Sahara
(15) 10/23 - 22:57	3.3	9	Spain origin - Long passage over the Mediterranean sea No significant aerosol layer

664

665 Table 3: Same as Table 2 for the ChArMEx experiment (2013 summer period).

(CN) Month/Day - LT	<i>D</i> (km)	<i>N</i>	Observation
(1) 06/10 - 21:59	5.8	12	Spain - Southern France origin Strong subsidence from ~6 to 2 km
(2) 06/11 - 23:18	7.2	12	Atlantic - Spain origin RPL from Barcelona coast
(3) 06/12 - 22:57	3.5	12	Atlantic - Spain origin Strong subsidence from ~8 to 5 km
(4) 06/13 - 22:36	5.0	12	Atlantic-Southern France origin RPL from Perpignan coast Dry air mass at ~3 km (drying over the Pyrenees)
(5) 06/14 - 22:15	2.2	12	France origin below 1 km Tropical Atlantic - Southern Spain origin above 1 km RPL from Valencia coast
(6) 06/15 - 21:54	4.4	12	Mediterranean origin below 1 km Atlantic (off Moroccan coast) - Southern Spain origin above 1 km DL between ~2.5 and 4 km
(7) 06/16 - 23:15	11.2	12	Mediterranean origin below 1 km Morocco-Algeria origin above 1 km DL between 1 and 5 km
(8) 06/17 - 22:54	4.0	10	Atlantic - Morocco origin with a small DL ~0-7 km. Likely dust uptake between 0 and 4 km
(9) 06/20 - 23:33	47.1	12	Spain origin RPL from Valencia coast
(10) 06/22 - 22:51	3.0	12	Atlantic - Spain - Southwestern France origin Strong subsidence between ~9 and 4 km RPL from Barcelona coast
(11) 06/24 - 22:09	8.2	12	Atlantic - Spain - Southwestern France origin Strong subsidence between ~7 and 0 km Dry air mass at ~2.5 km RPL from Barcelona coast
(12) 06/25 - 23:27	29.0	12	Atlantic - Spain - Southwestern France origin Strong subsidence between ~8 and 4 km RPL from Perpignan coast
(13) 06/27 - 22:48	14.3	6	Northern Atlantic - France origin RPL from Perpignan coast
(14) 06/30 - 23:24	19.4	12	Northwestern Atlantic - France origin
(15) 07/02 - 22:42	4.2	10	France - Spain - Morocco origin with a DL between 3 and 5 km Strong wind-shear - RPL from Montpellier and Barcelona coasts

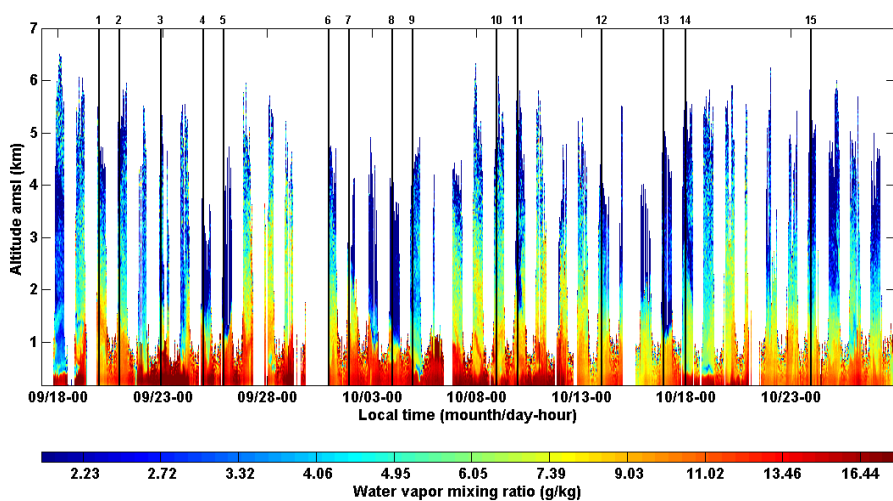
666

667 Table 4: Scores on the WVMR retrieval for the inter-comparisons between WALI and IASI
 668 (WALI-IASI), and WALI and ECMWF (WALI-ECMWF). The results are given for different
 669 atmospheric layers in terms of COR and RMSE for the two time periods.

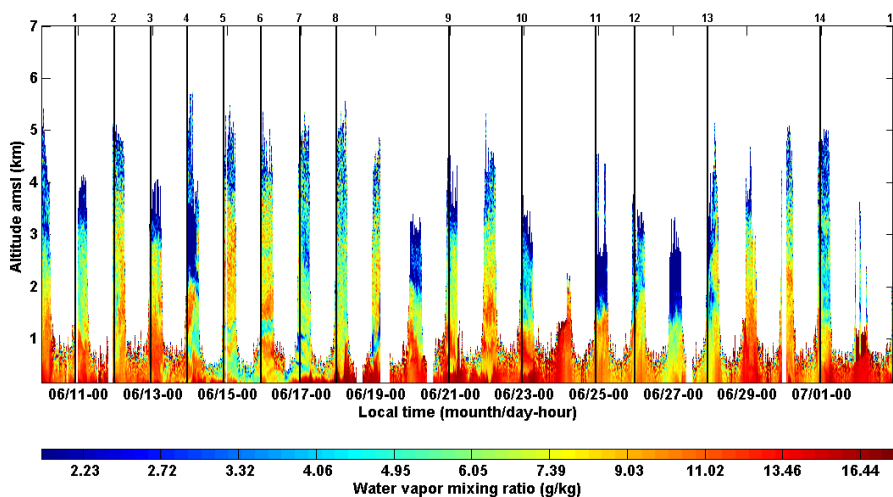
Altitude range (km)	COR		RMSE (g/kg)	
	WALI-IASI	WALI-ECMWF	WALI_IASI	WALI-ECMWF
September-October 2012				
0.5-2.0	0.37	0.73	1.42	1.15
2.0-5.0	0.77	0.81	0.66	0.55
5.0-7.0	0.78	0.73	0.25	0.26
0.5-7.0	0.70	0.77	0.78	0.65
June-July 2013				
0.5-2.0	0.15	0.74	1.80	2.42
2.0-5.0	0.70	0.91	1.34	1.16
5.0-7.0	0.75	0.77	0.67	0.66
0.5-7.0	0.59	0.82	1.28	1.43

670

671



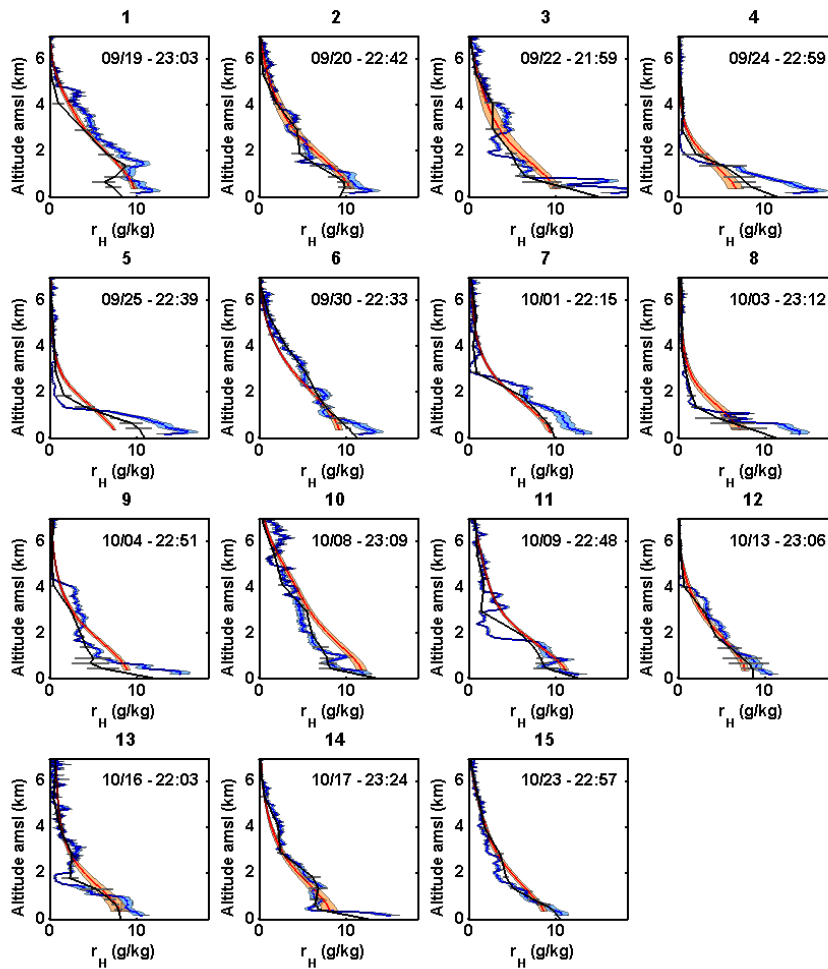
672



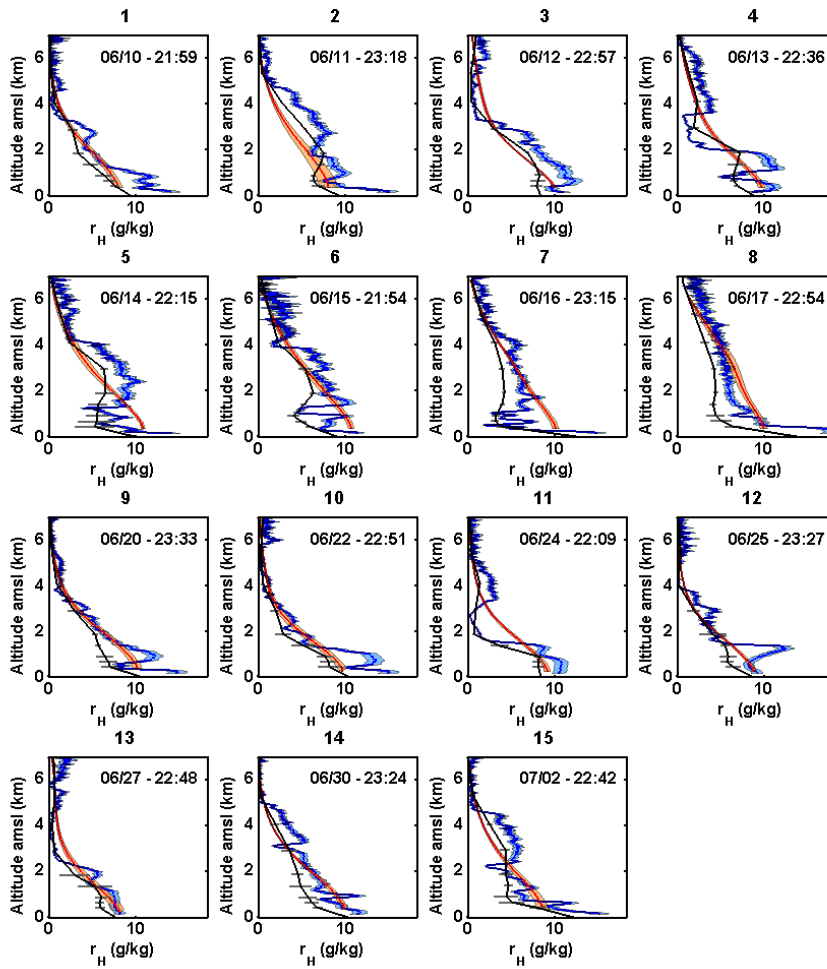
673

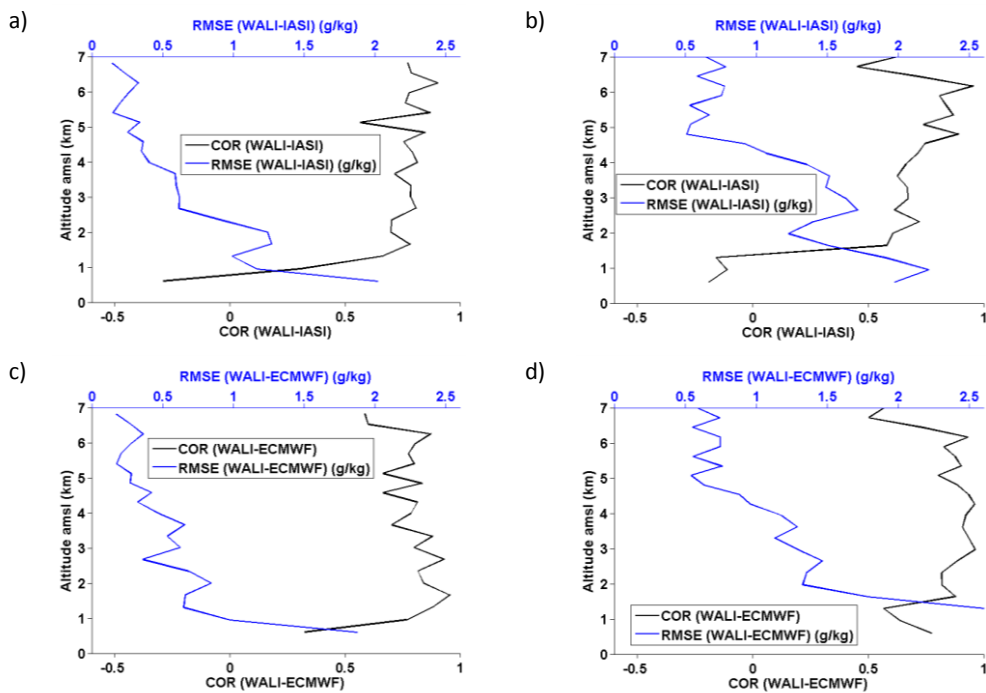
674 Figure 1: Time localization of the IASI profiles used for the inter-comparisons (vertical black
 675 lines identified with the CN at the top) with respect to the temporal WALI lidar WVMR (in
 676 g/kg) retrieval evolution as a function of altitude (in km) during the HyMeX (up) and
 677 ChArMEx (down) periods. lidar profiles are given with a high temporal resolution of 5
 678 minutes averaging. The color bar ranges from low water vapor mixing-ratio (blue) to high
 679 ones (red).

680

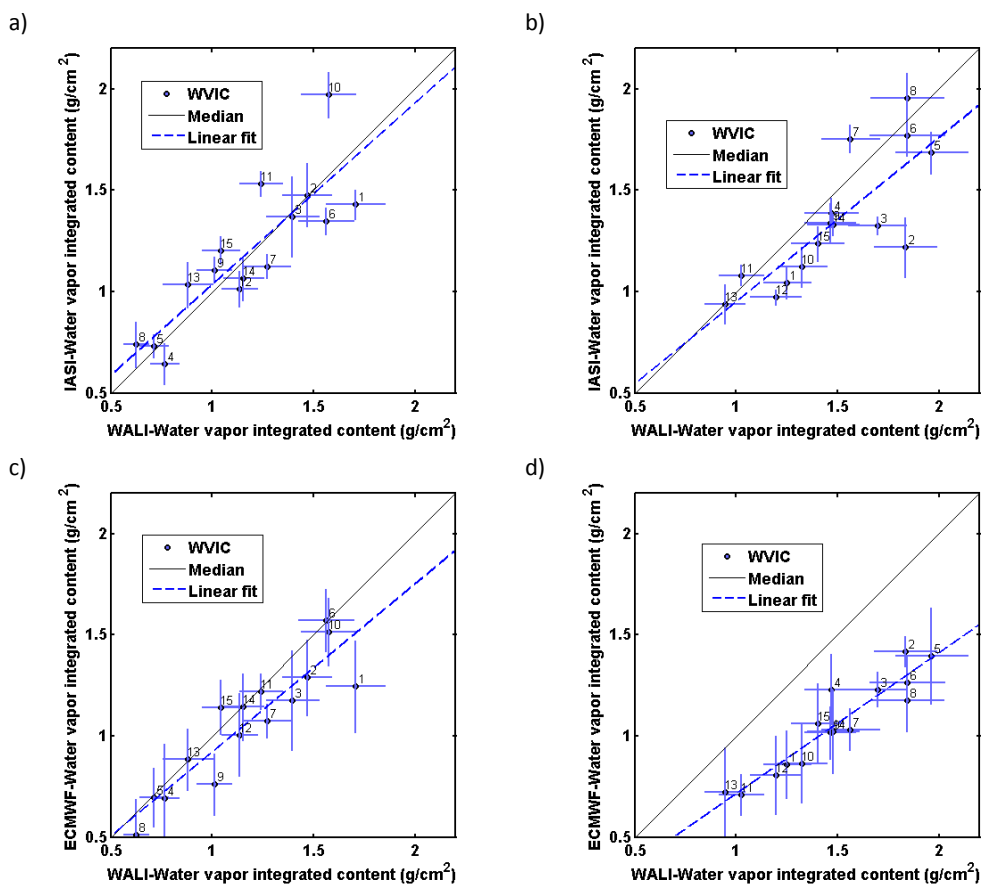


683 Figure 2: Comparisons of WVMR vertical profile retrieval as a function of altitude between:
 684 IASI (red), WALI lidar (blue) and ECMWF analysis (black), over Menorca during the
 685 HyMeX experiment (September and October 2012). The date and time of the IASI and WALI
 686 measurements are also given for each panel of individual profile in the form month/day
 687 HH:MM. The CN is given at the top of each figure.





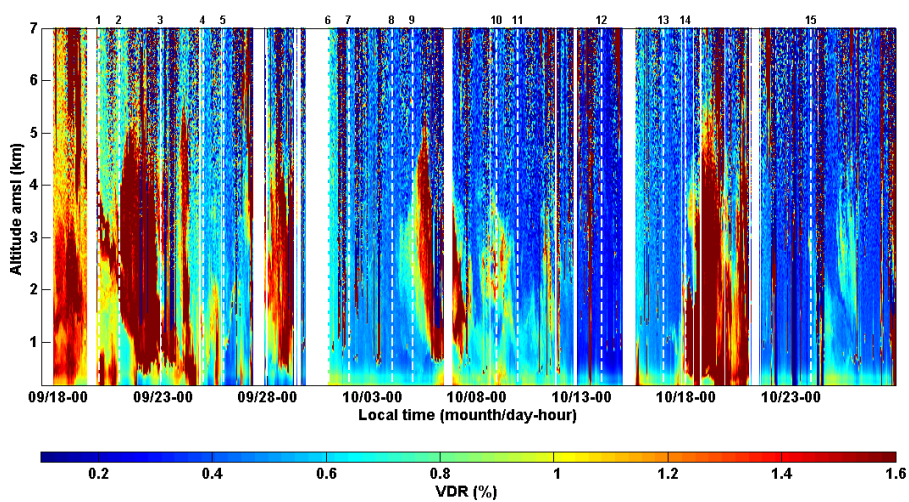
691 Figure 4: Evolution as a function of altitude of the RMSE in g/kg (blue) and COR between
 692 IASI and WALI WVMR retrievals for HyMeX (a) and ChArMEx (b) periods, and between
 693 WALI WVMR retrieval and ECMWF analysis for HyMeX (c) and ChArMEx (d) periods.



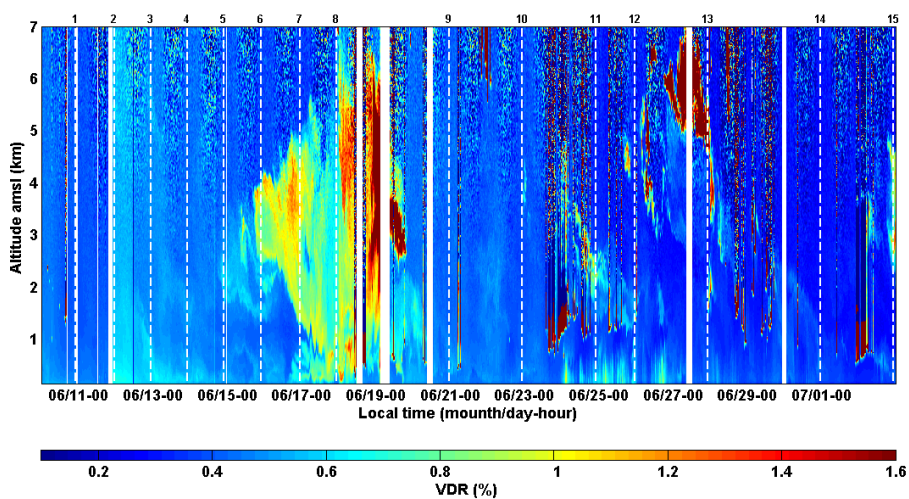
694

695 | Figure 5: Water Vapor Integrated Content (WVIC in g/cm²) as measured by WALI lidar
 696 | against IASI WVIC retrieval for HyMeX (a) and ChArMEx (b) periods and against ECMWF
 697 | WVIR for HyMeX (c) and ChArMEx periods (d). Line styles are given in each individual
 698 | figure legends.

699



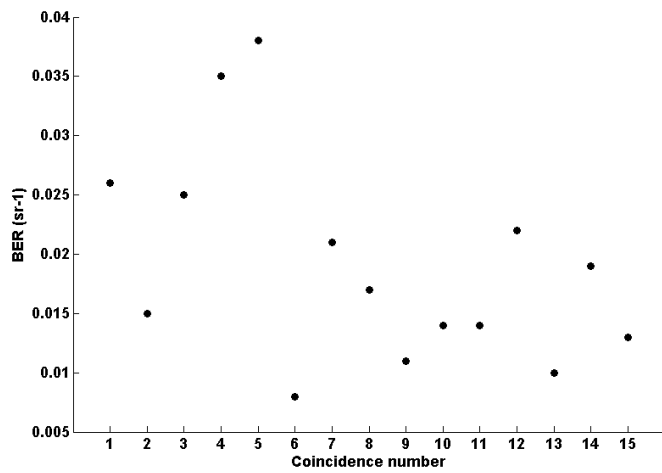
700



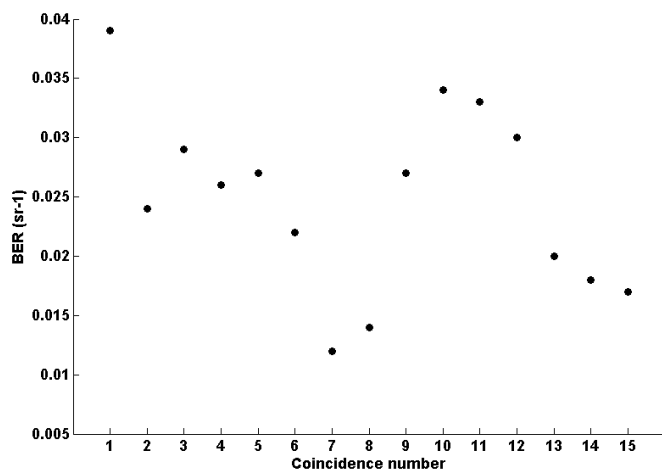
701

702 Figure 6: Volume Depolarization Ratio (VDR in %) evolution as a function of altitude (in km)
703 during HyMeX (up) and ChArMEx (down) experiments comparisons. The vertical white
704 dotted lines identify the coincidences with the CN at the top. The color bar ranges from low
705 VDR (blue) to high ones (red).

706

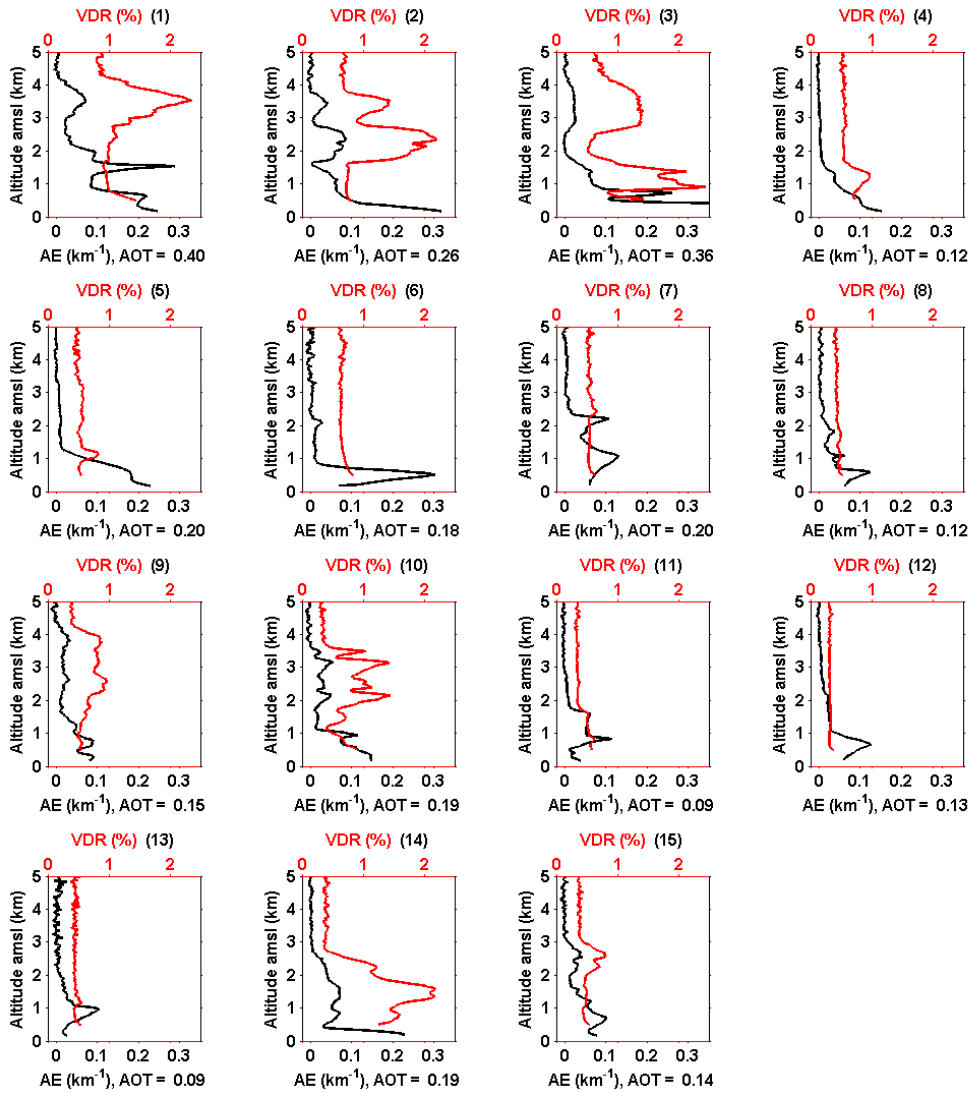


707

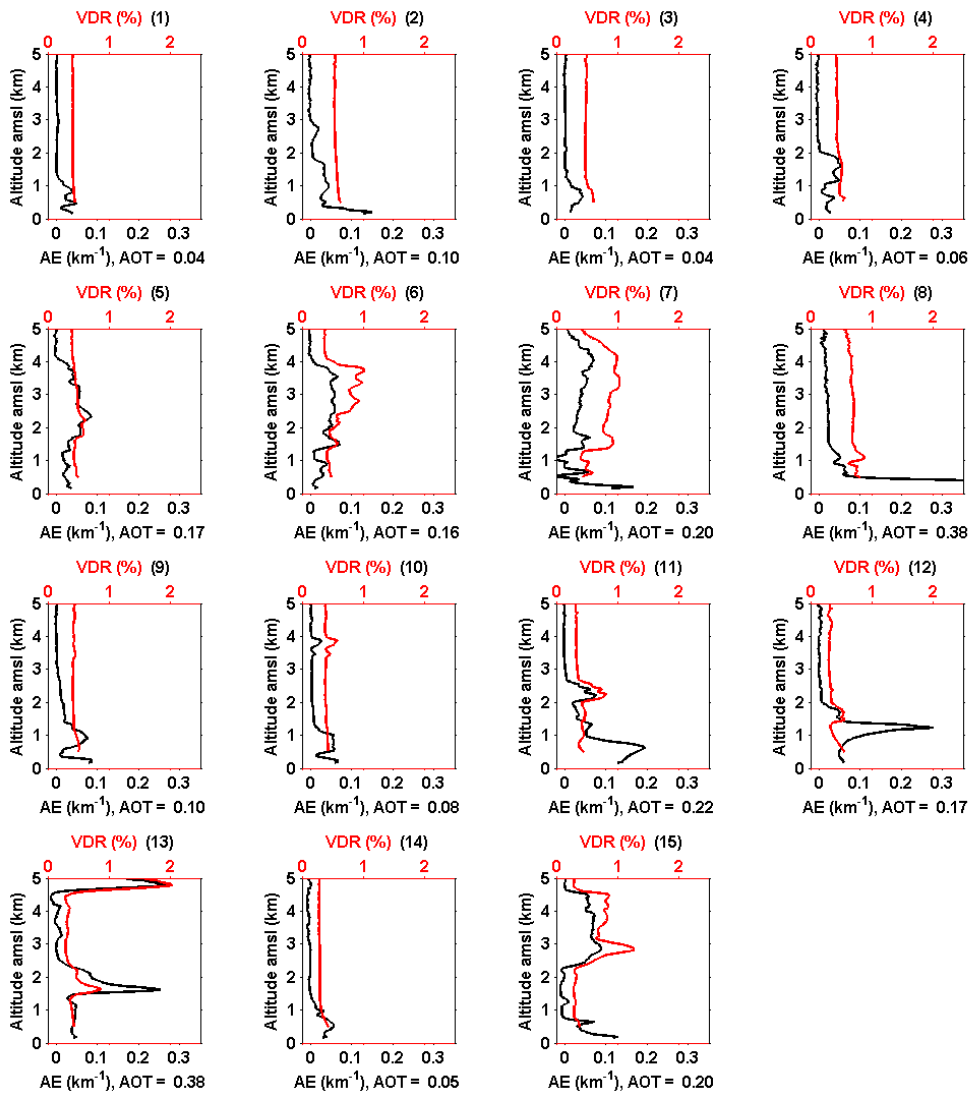


708

709 Figure 7: Column Backscatter to Extinction Ratio (BER in sr⁻¹) derived from WALI temporal
 710 evolution for the different inter-comparisons exercises during HyMeX (up) and ChArMEX
 711 (down) experiments. Abscisa represents the CN.

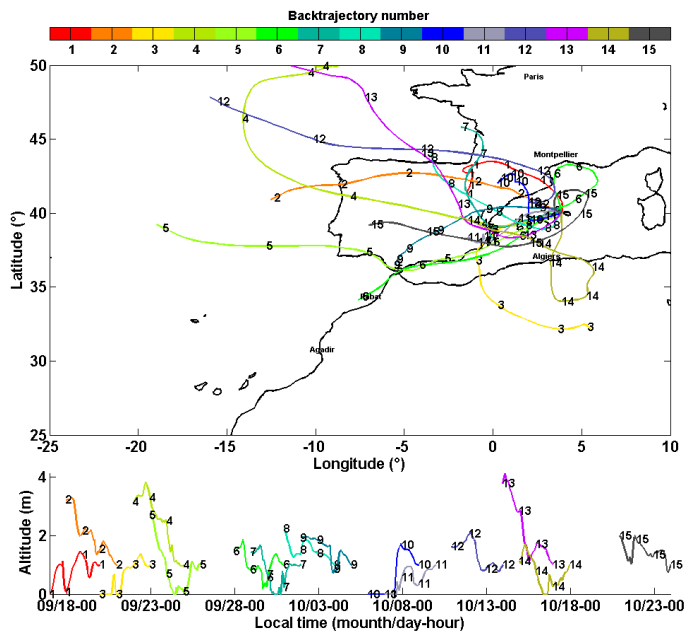


712
 713 Figure 8: Aerosol extinction coefficient (AE in km⁻¹, black lines) and Volume Depolarization
 714 Ratio (VDR in %, red lines) as a function of altitude for the inter-comparisons cases during
 715 HyMeX experiment. For each individual case, the Atmospheric Optical Thickness (AOT) is
 716 also reported. The CN is given in black at the top of each figure.

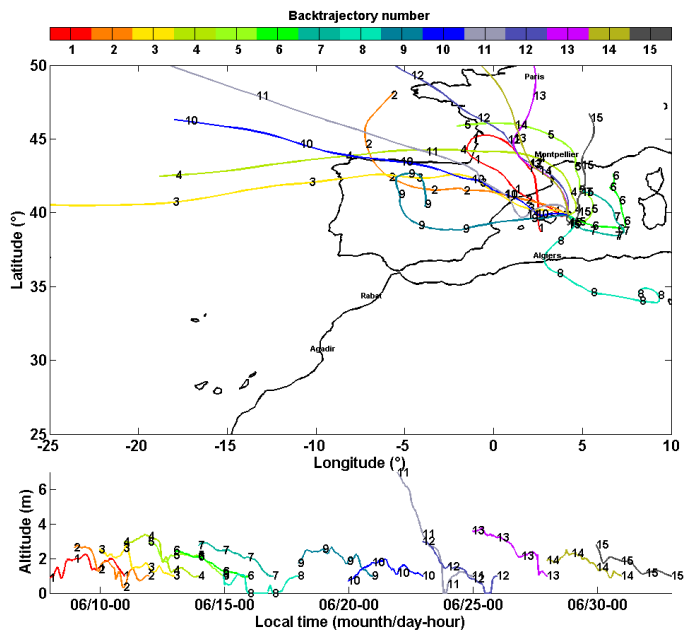


718

719 | Figure 9: Same as Figure 8 for the ChArMEx experiment (June and July 2013).

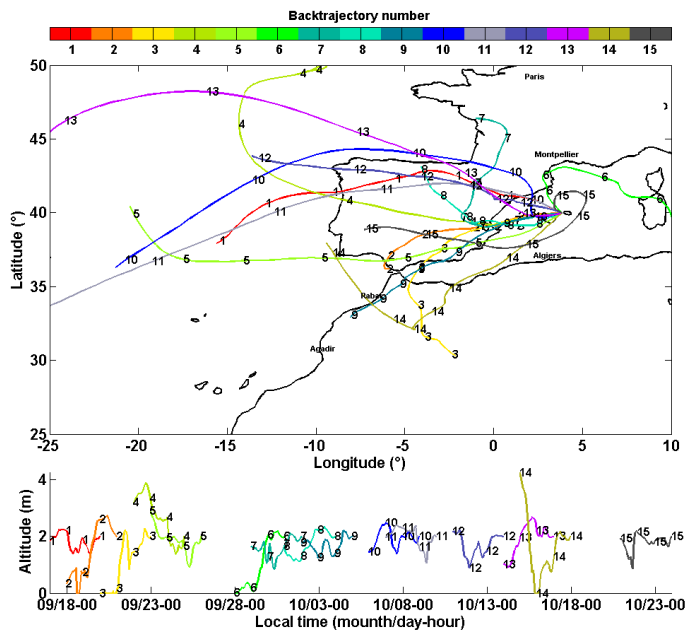


720

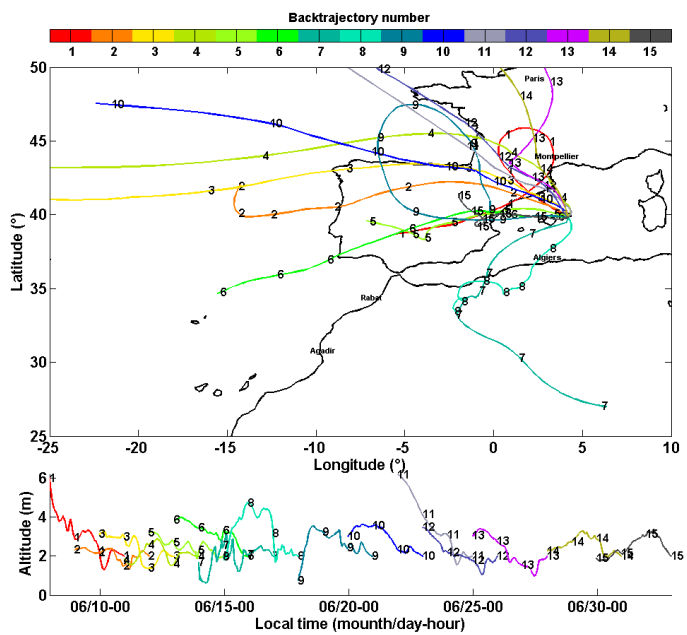


721

722 Figure 10: Back trajectories for each CN. They have been computed using the Hysplit model
 723 (courtesy of NOAA Air Resources Laboratory; <http://www.arl.noaa.gov>). The end locations
 724 of the air masses are for the sites of Ciutadella (up) and Mahon (down) for the HyMeX and
 725 ChArMEx time periods, respectively, at the altitudes of 1 km amsl.



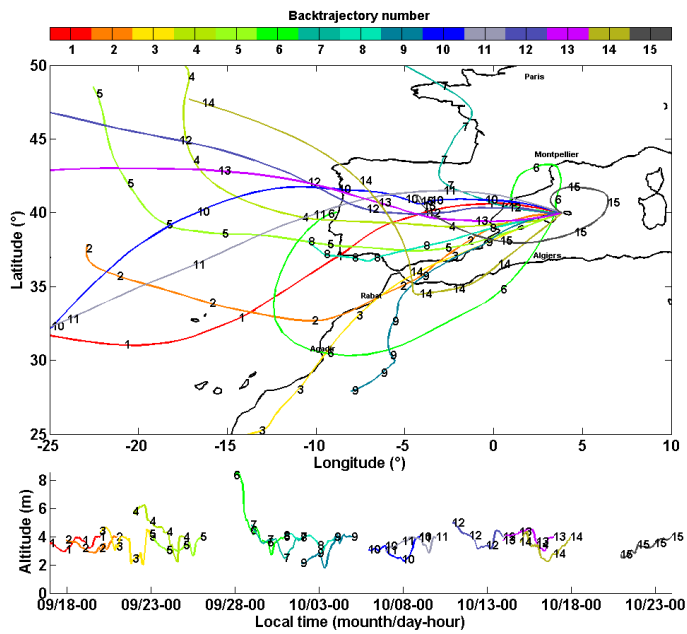
726



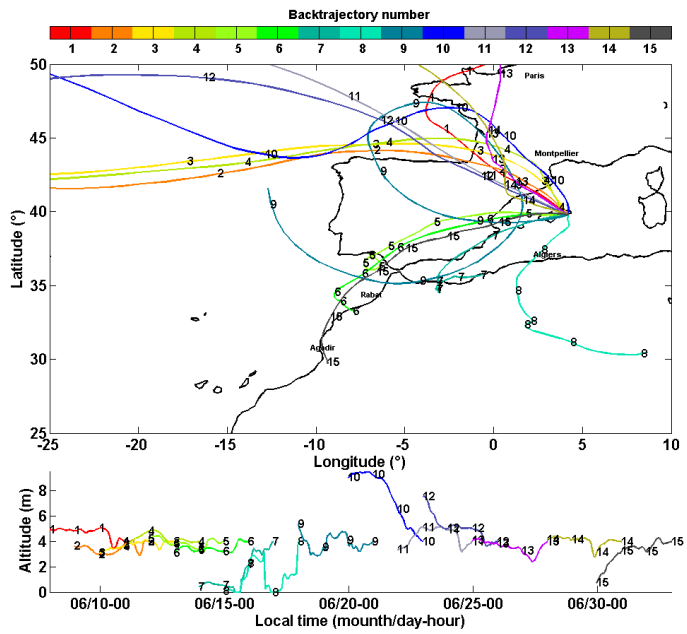
727

728 | Figure 11: Same as Figure 10 for 2 km amsl.

729



730



731

732 | Figure 12: Same as Figure 10 for 4 km amsl.